A Multibody Modeling Approach Applied to the Redesign for Additive Manufacturing of a Load Bearing Structure

applied sciences

MDPI

Article

A Multibody Modeling Approach Applied to the Redesign for Additive Manufacturing of a Load Bearing Structure

Davide Sorli [1,*], Paolo Minetola [1] and Stefano Mauro [2]

[1] Department of Management and Production Engineering, Politecnico di Torino, 10129 Torino, Italy; paolo.minetola@polito.it
[2] Department of Mechanical and Aerospace Engineering, Politecnico di Torino, 10129 Torino, Italy; stefano.mauro@polito.it
* Correspondence: davide.sorli@polito.it

Abstract

This study addresses the critical need to enhance productivity in industrial automatic systems by optimizing the mass of moving components. The primary challenge is determining the complex, dynamic loads on structural elements, a prerequisite for effective redesign, without access to physical prototypes for experimental measurement. This paper presents a solution through a case study of a load-bearing pylon in a fine blanking plant, which is subject to inertial loads and shocks from pneumatic actuators and shock absorbers. To overcome this challenge, a high-fidelity multibody simulation model is developed to accurately estimate the dynamic loads on the pylon. This data is given as input to the topology optimization (TO) process, following the Design for Additive Manufacturing (DfAM) framework, to redesign the pylon for mass reduction using a Powder Bed Fusion-Laser Beam (PBF-LB). Two materials, EOS Aluminum Al2139 AM and EOS Maraging Steel MS1, are evaluated. The findings demonstrate that the integrated simulation and redesign approach is highly effective. The redesigned pylon's performance is verified within the same simulation environment, confirming the productivity gains before manufacturing. A cost analysis revealed that the additively manufactured solution is more expensive than traditional methods, and the final choice depends on the overall productivity increase. This research validates a powerful methodology that integrates dynamic multibody analysis with topology optimization for AM. This approach is recommended in the design phase of complex industrial machinery to evaluate and quantify performance improvements and make informed decisions on the cost-effectiveness of introducing AM components without the need for physical prototyping.

Keywords: multibody modeling; DfAM; topology optimization; contact mechanics; PBF-LB

Academic Editor: Arkadiusz Gola

Received: 18 July 2025
Revised: 18 August 2025
Accepted: 21 August 2025
Published: 25 August 2025

Citation: Sorli, D.; Minetola, P.; Mauro, S. A Multibody Modeling Approach Applied to the Redesign for Additive Manufacturing of a Load Bearing Structure. *Appl. Sci.* **2025**, *15*, 9312. https://doi.org/10.3390/app15179312

1. Introduction

Additive manufacturing (AM) technology is known as a flexible and versatile manufacturing process that allows the designer to consider different solutions compared to traditional manufacturing techniques. The technology has evolved over the years from rapid prototyping applications for evaluating design functionality [1] to the creation of highly specialized prosthetic elements in the biomedical industry [2]. As the technology has evolved, AM techniques have been adopted in a variety of fields, from automotive to aerospace, with solutions ranging from rapid prototyping to low-volume component production [3]. AM is a mature manufacturing technique to produce market-ready metallic

components [4]. Several metal AM technologies have been established as industrial processes [5,6]. Among others, the Laser Powder Bed Fusion-Laser Beam (PBF-LB) process has demonstrated its capability to produce components with low porosity [7] and high-quality finishing [8]. To apply PBF-LB for the production of structural components, a heat treatment process is usually necessary to improve the strength properties of the material [9,10].

The advantages offered by AM techniques concern the freedom in terms of the geometries that can be realized, leading to the application of AM techniques for the production of lightweight designs [11]. These characteristics have also led to the application of these techniques in the industrial sector, where the ability to optimize load-bearing elements is appreciated, leading to improved plant efficiency [12]. The optimization of structural elements often involves the use of topological optimization (TO) techniques, which rely on various optimization methods [13] and can be applied to a variety of systems [14,15]. In a recent review [16] it is highlighted the interest in TO and AM in industrial applications. TO potentiality is fully realized when coupled with AM and Design for Additive Manufacturing (DfAM) [17]. The literature highlights a great interest in the DfAM topic [18,19]. In the DfAM process, the designer performs a series of iterative operations [20]. The component under study is analyzed by the finite element method (FEM), the geometry is optimized by TO software, and the result is interpreted in CAD format, and finally verified by a second FEM analysis. The product development process is shown in Figure 1 [20]. There are examples of the application of this workflow to load-bearing components used in industry [21]. In [22], the authors proposed a novel methodology of DfAM aimed at choosing the best manufacturing process for a specific scenario, with special attention on the distinction between AM and conventional processes. Using an aircraft structural bracket, authors demonstrate that AM process are ideal for the production of small batches and highlight the positive role that TO may fill.

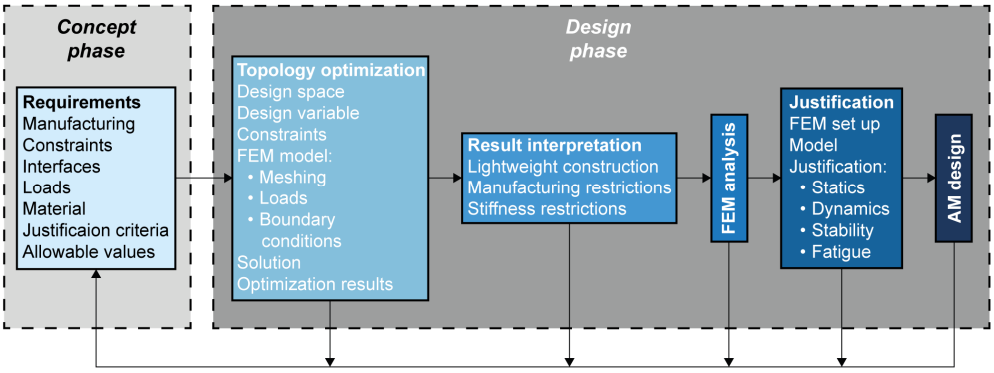

Figure 1. Redesign for additive manufacturing workflow [20].

The first phase of the DfAM process involves the definition of requirements: manufacturing restrictions, interfaces, material(s), loads, and justification criteria [17]. For load-bearing components, the justification criteria typically involve minimizing mass and/or maximizing stiffness [23]. To perform the load analysis on a load-bearing component for systems involving multiple contact interactions, it can be useful to employ dedicated multibody simulation software [24]. In [25], the multibody modeling approach is used in the mechatronic system of an automotive suspension to evaluate the forces exchanged between wheels and the ground. In [26], the torques expressed at the joints of a UR5 robotic manipulator are evaluated using the multibody approach, and validated with experimental results. In systems where multiple contacts occur, it can be useful to use dedicated multibody software. In [27], the model of a nut ball screw is built in the MSC Adams environment to evaluate the effects of ball jamming in the recirculating channel.

The literature analysis shows that multibody modelling is a mature technique that allow designers to evaluate the behavior of complex multi-domain systems [28].

However, based on the literature review conducted, it was found that there is little integration of dynamic analysis techniques for the study of components in AM, where research often focuses more on TO [29,30] and process optimization aspects [31,32]. In [33], the multibody modeling approach is applied to the TO of a flexible load-bearing element. In [34] can be found an example of integration of dynamic analysis and DfAM applied to a suspension knuckle redesigned to maximize the stiffness. However, there is a lack of studies about this approach applied to industrial systems.

The primary objective of this research is to develop and test, on a case study, an integrated methodology to analyze the opportunities offered by TO and DfAM to improve the performance of a manufacturing plant and reduce the production cost. The methodology combines high-fidelity multi-body dynamic simulation with DfAM and TO techniques. This study addresses a critical gap where dynamic operational loads, essential for effective optimization, are unknown, particularly for industrial systems not yet physically prototyped. The specific goals are to (1) accurately predict these dynamic loads on a structural component, using a multi-body model, considering as a case study a fine blanking plant; (2) use this data to redesign and minimize the component's mass via TO for PBF-LB; and (3) quantitatively evaluate the resulting improvements in system performance and productivity before committing to manufacturing, thereby creating a closed-loop virtual validation process. The developed model will also be used to verify a posteriori the actual performance improvement as a result of the DfAM process, allowing a future evaluation of the cost-effectiveness of introducing AM into the design process of this type of devices.

This paper is structured as follows: Section 2 describes the optimization methodology, detailing the case study, the development of the pneumatic and multi-body models, and the process for determining contact model parameters. Section 3 presents the topology optimization process, from the initial results to the final DfAM solution, including validation through FE analysis. Section 4 provides a detailed cost analysis of the AM-produced components. Finally, Section 5 discusses the conclusions of the study, summarizing the findings and outlining the implications for industrial applications.

2. Optimization Methodology

For industrial mass production applications, one of the primary drivers for decisions is cost-effectiveness, making plant productivity a critical parameter. In high-speed automated systems, productivity is directly correlated with the dynamic behavior of its moving parts; minimizing moving masses can decrease cycle time and thus increase output.

This work proposes a systematic methodology to achieve and verify this optimization virtually, prior to manufacturing. The technical roadmap for this methodology is as follows:

1. Machine analysis: The components of a high-speed automated system under design are analyzed to identify which components are most suitable for the proposed optimization methodology. The analysis must focus on moving components that are most massive and have structural purposes.
2. Dynamic Load Determination: a high-fidelity simulation model is developed. This involves co-simulating a multi-body model of the mechanical system in Adams and the model of the actuators in Matlab/Simulink to determine the precise, transient loads acting on the mechanical parts suitable for optimization.
3. Optimization: The load data obtained from the simulation are used as a direct input for a Topology Optimization (TO) study. The TO results are then interpreted using DfAM principles to create a manufacturable geometry for the Laser Powder Bed Fusion (PBF-LB) process.

4. Performance Verification: The novelty of this work lies in closing the optimization loop. The final, optimized geometry is re-introduced into the multi-body model to simulate the new system dynamics and quantitatively verify the improvement in cycle time and productivity.
5. Cost Analysis: Finally, a detailed cost analysis is conducted to evaluate the economic feasibility of the AM solution compared to traditional methods, providing a comprehensive assessment of its overall value.

This method is applied to the case study of a load-bearing pylon in a device used in a fine blanking plant under design at the Util Industries group.

3. Case Study

The analyzed system is utilized in an industrial plant to remove fine blanket products from the press area. Figure 2 displays the main components of the system. The movement is kept translational by a pair of prismatic guides (c). Once the product (f) is ejected from the die, it is gripped by the transfer plate (a) and evacuated outside the press area. The movement is transmitted from two pneumatic actuators (e) to the plate by structural pylons (b). To prevent collisions with the end stops, shock absorbers (d) dissipate the system's kinetic energy at the end of the stroke.

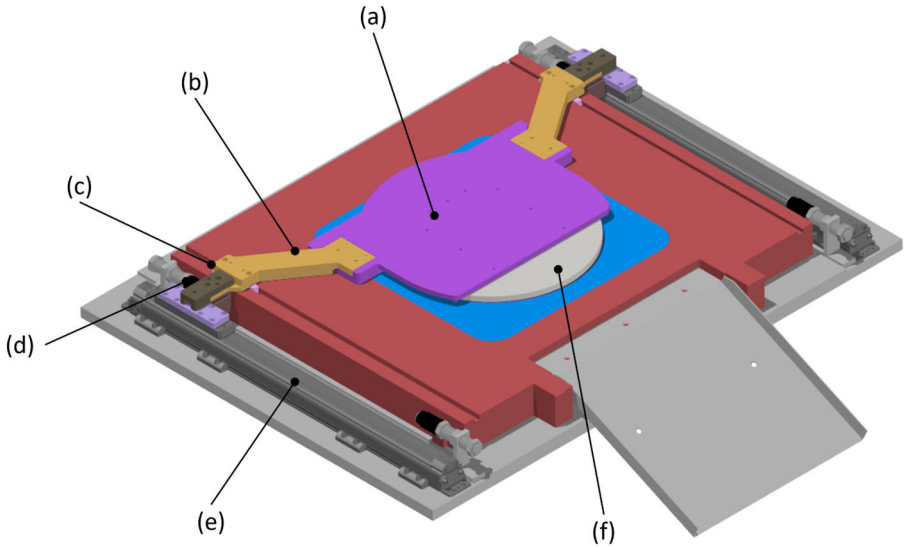

Figure 2. System description: (a) transfer plate, (b) load-bearing pylon, (c) prismatic rail guide, (d) shock absorber, (e) pneumatic actuator, (f) product.

The operating cycle of the transfer device (Figure 2) begins when the fine blanking press cycle reaches the point of die opening. The device travels twice, first to position the transfer plate on the product, and then to evacuate the product by grasping it and moving it outside the press area. For the operating cycle of the transfer device, two impacts occur between the translating end stops and the shock absorbers: the first at the end of the positioning phase and the second at the end of the product evacuation phase.

The time required for translation influences the cycle time and depends on the mass of the translated components, including both the product and the transfer device, and on the force applied by the actuator. To increase productivity, it is necessary to minimize the cycle time and, hence, the mass of the elements of the transfer device.

Table 1 summarizes the mass of the most relevant components of the transfer device. The most massive element is the transfer plate; however, its design and its material cannot be changed significantly due to its functional purpose. The pylon is the second-most massive component, serving only a structural purpose. The combined mass of the two

pylons represents approximately 31% of the total mass of the device. Therefore, optimizing the pylon's mass can significantly reduce the mass of the device, resulting in increased productivity. So the structural pylon was chosen as the case study for this work.

Table 1. Mass of the main components of the device.

Component	Mass (Kg)	Number of Components Present in the Device
Transfer plate	6.096	1
Structural pylon	2.595	2
End stop	0.803	2
...	...	
Total mass of the device	16.631	

To minimize the mass of the pylon, TO techniques are applied. However, it is necessary to know the loads acting on the components during the motion, which are dependent on the behavior of the pneumatic actuators, dampers, and friction. Analytical closed-form solutions for determining these forces are not possible due to the high dependence of the device's behavior on the transient of the pneumatic actuators. Therefore, this work proposes a numerical model of the pneumatic actuators, and a multibody model of the device to determine the forces exchanged between the system's elements, specifically the pylon and the transfer plate. The two models are used in co-simulation in order to evaluate the forces.

4. System Modeling

4.1. Pneumatic Model

The Matlab/Simulink environment is used to build the pneumatic actuator model [35]. The model includes the valve model, which accounts for sonic–subsonic behavior. The pneumatic line is modeled as a reservoir and restriction, while the pneumatic cylinder model takes in the air flow between chambers and the actuator displacement as input. The output includes the force generated by the actuator and the pressure in the chambers, allowing for the dynamic behavior of the cylinder to be modeled. As the device is intended to use two actuators, the model has been duplicated to include them both. The parameters for the characteristics of the components included in the model come from the datasheet of the transfer device components and are shown in Table 2.

Table 2. Pneumatic model parameters.

Valve Parameters	Value
Conductance (Nm^3/sPa)	4.49×10^{-8}
Critical ratio	0.19
Pneumatic Line Parameters	**Value**
Source pressure (kPa)	700
Volume (m^3)	3×10^{-5}
Conductance (Nm^3/sPa)	1.68×10^{-8}
Critical ratio	0.4

The air used in the plant is at the pressure of 7 bar; the relief air is considered having standard conditions.

In Figure 3 is represented the pneumatic model of the actuator in the Matlab/Simulink environment.

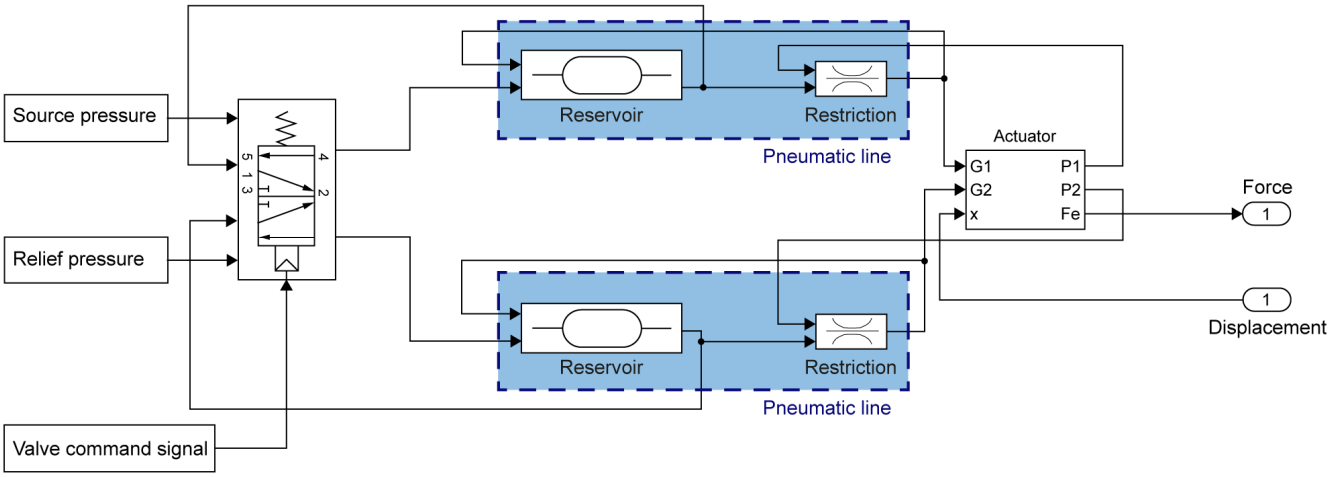

Figure 3. Model of the pneumatic actuator system.

4.2. Multibody Model

In a multibody model, rigid or flexible bodies are connected by kinetic and dynamic constraints. The model consists of two assemblies: one fixed to the ground and one translating.

A joint is necessary to calculate the forces exchanged between two rigid bodies. A decision must be made regarding the modeling of the rail guide system. The rails' behavior is described by applying a contact constraint between the moving rail and the fixed guide, which allows a better modeling than using a simpler translational prismatic joint model [36]. Additionally, contact constraints are applied between the product and the fixed base, as well as between the product and the transfer plate. The shock absorbers are modeled as spring-damper systems, with their characteristics identified by their technical datasheet [37]. Shock absorbers are implemented in the multibody model, as their behavior can be well described using a contact constraint between the shock absorber and the translating reference.

4.3. Contact Model

Contact is modeled using a viscoelastic function defined by four coefficients, as described in [38,39]. The contact force is calculated as:

$$F_C = k(q_0 - q)^e - C_{max}\dot{q} \cdot STEP(q, q_0 - d, 1, q_0, 0) \quad (1)$$

where:

- k: Stiffness coefficient: the coefficient of the elastic component of the contact force; it depends on both the material properties and the contact geometry.
- e: the exponent introduces the nonlinearity in the elastic component of the contact force; it depends on the material hardness.
- C_{max}: Damping coefficient: the coefficient associated with the viscous component of the contact force; it has no theoretical computation but must be chosen in relation to the stiffness coefficient.
- q: Penetration depth: the penetration depth has no physical meaning but the purpose is to keep the damping continuous during the onset of contact.

Additionally, the friction is included using a continuous friction model defined by a STEP function with four parameters [38].

- μ_d: Dynamic friction coefficient: specifies the coefficient of friction at the contact point when the slip velocity is higher than V_d.

- μ_s: Static friction coefficient: specifies the coefficient of friction at the contact point when the slip velocity is lower than V_s.
- V_d: Dynamic transition velocity: The friction coefficient is gradually transitioned from the μ_s to the μ_d as the slip velocity at the contact point increases. When the slip velocity is equal to the value specified for V_d, the effective coefficient of friction is set to μ_d.
- V_s: Static transition velocity: The friction coefficient is gradually transitioned from the μ_d to μ_s as the slip velocity at the contact point decreases. When the slip velocity is equal to the value specified for V_s, the effective coefficient of friction is set to μ_s.

It is important to note that the contact parameters depend on the materials of the parts in contact and also on their geometries. This is because the contact reaction force is determined using the centroid of the penetration volume.

A precise identification of these parameters usually requires an experimental setup, which is not possible at the time of this study, and is not generally suitable in a design phase. However, it is possible to estimate them through an influence analysis performed in the multibody environment [40]. For the case study presented, an influence analysis of the stiffness is performed, damping and exponent, while the influence of the penetration depth parameter has not been investigated because its order of magnitude can be estimated from the literature as 0.01 mm [39].

4.4. Contact Parameters Influence

A precise identification of the contact model parameters would typically require a dedicated experimental setup. However, as this is often not feasible during the early design phase, an efficient approach consists in performing a systematic influence analysis within the multibody environment to determine appropriate and conservative values. This approach, guided by established literature and software documentation, ensures the selection of robust parameters by evaluating the sensitivity of the model's key output, the peak force on the pylon, to variations in each parameter.

Each parameter is evaluated at three different levels. The model output taken as a reference is the peak force at the pylon–transfer plate joint, which is the main output of the multibody model. The range of values varying of the parameters is defined through a literature analysis of the most likely correct values indicated for the case of systems such as the one studied [40]. First, the contact stiffness coefficient is evaluated, considering 10^4 N/mm, 10^5 N/mm, and 10^6 N/mm. The model results (Figure 4) show that the force exchanged at the joint is not significantly affected by the value of the stiffness coefficient. The contact stiffness is then chosen as 10^5 N/mm, which is the suggested value according to the Adams 2020 software user's guide [38].

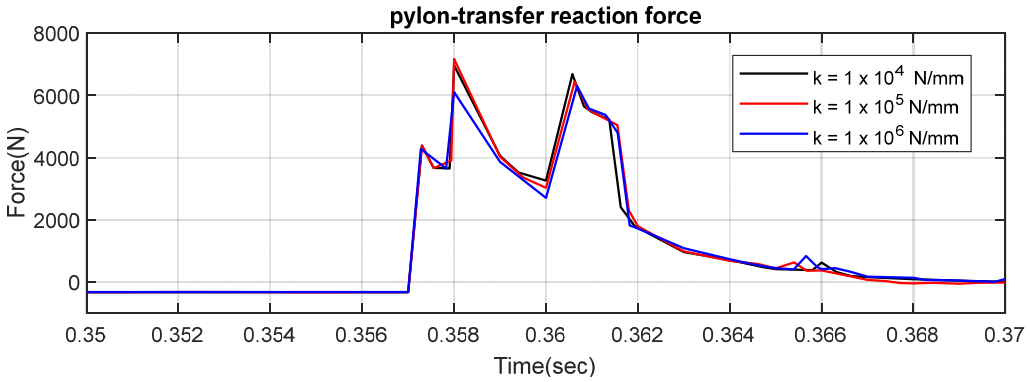

Figure 4. Influence of the stiffness coefficient on the pylon load.

According to literature, the damping coefficient is suggested to be 10^{-3} of the stiffness. Values of 10 Ns/mm, 100 Ns/mm, and 1000 Ns/mm are considered for sensitivity analysis. The results (Figure 5) show that, despite minor changes in behavior, the magnitude of the force peak does not change substantially with the different values. Conservatively, a contact damping value of 1000 Ns/mm is chosen, as it leads to the highest peak force.

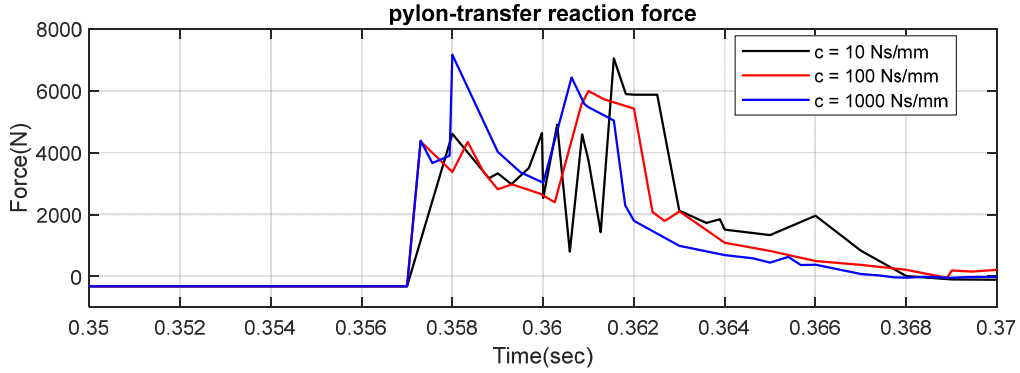

Figure 5. Influence of the damping coefficient on the pylon load.

The force exponent is correlated with the material hardness. In this case, the device is made of hardened tool steel, so the force exponent is expected to close to 2.2. Values of 1.5, 1.7, and 2.2 are considered for sensitivity analysis (Figure 6); it is found that that the peak is higher for the lowest level of the exponent. However, it should be noted that the variation in the peak force is lower than 10% of its value, and that a value of 1.5 is not representative of the behavior of hardened steel contact. Therefore, the value of 2.2 was chosen for further analysis.

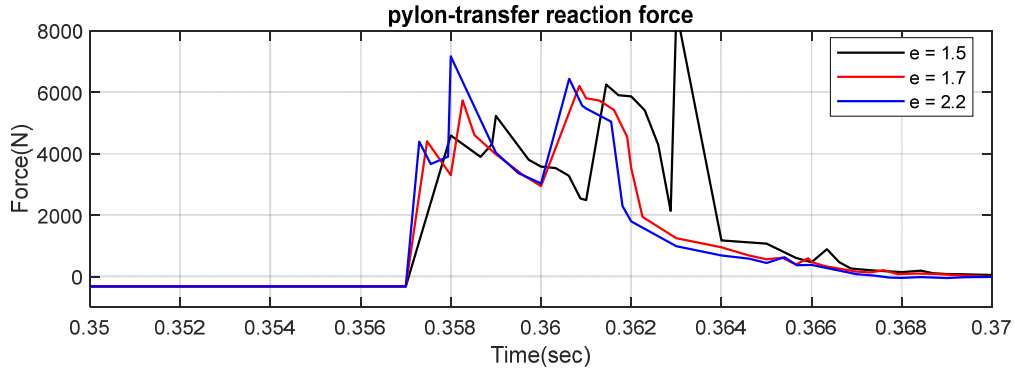

Figure 6. Influence of the contact function exponent on the pylon load.

4.5. Preliminary Results

The resulting model integrates the pneumatic system in Simulink with the multi-body model in Adams. The model operates through co-simulation, led by the Matlab/Simulink solver.

Simulations are performed considering the first command for valve commutation at time t = 0 and a second commutation after 0.5 s. The transfer plate's position is zero when it is in the product evacuation position, and it is negative during translation.

The force exchanged between the transfer plate and structural pylon can be evaluated using the results of the model simulation.

The pneumatic actuator force is shown in Figure 7.

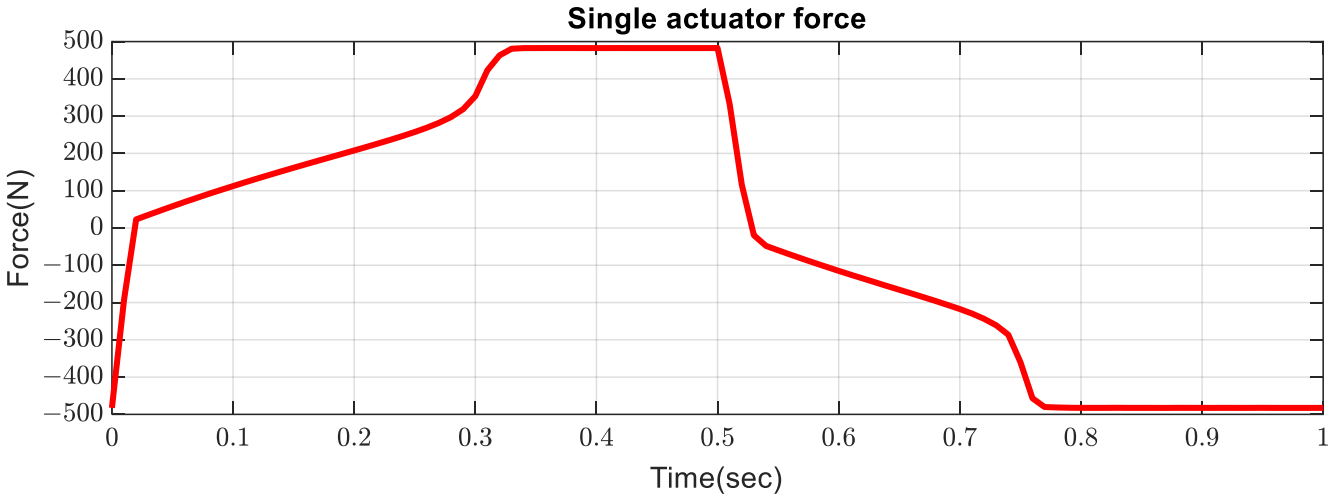

Figure 7. Actuator force.

In Figure 8, the force exchanged at the joint between the pylon and the transfer plate exhibits two peaks that correspond to the impact of the translating end-stop with the hydraulic shock absorber. The first peak is observed at the end of the product evacuation phase, while the second peak is observed at the end of the product grasping phase. Although the plant operates in a chronological sequence of phases, starting with the product grasping phase followed by the product evacuation phase, for simulation purposes, the two phases have been inverted. The reason for this choice is to observe the behavior of the whole system with only one simulation, without significantly affecting the quality of the results.

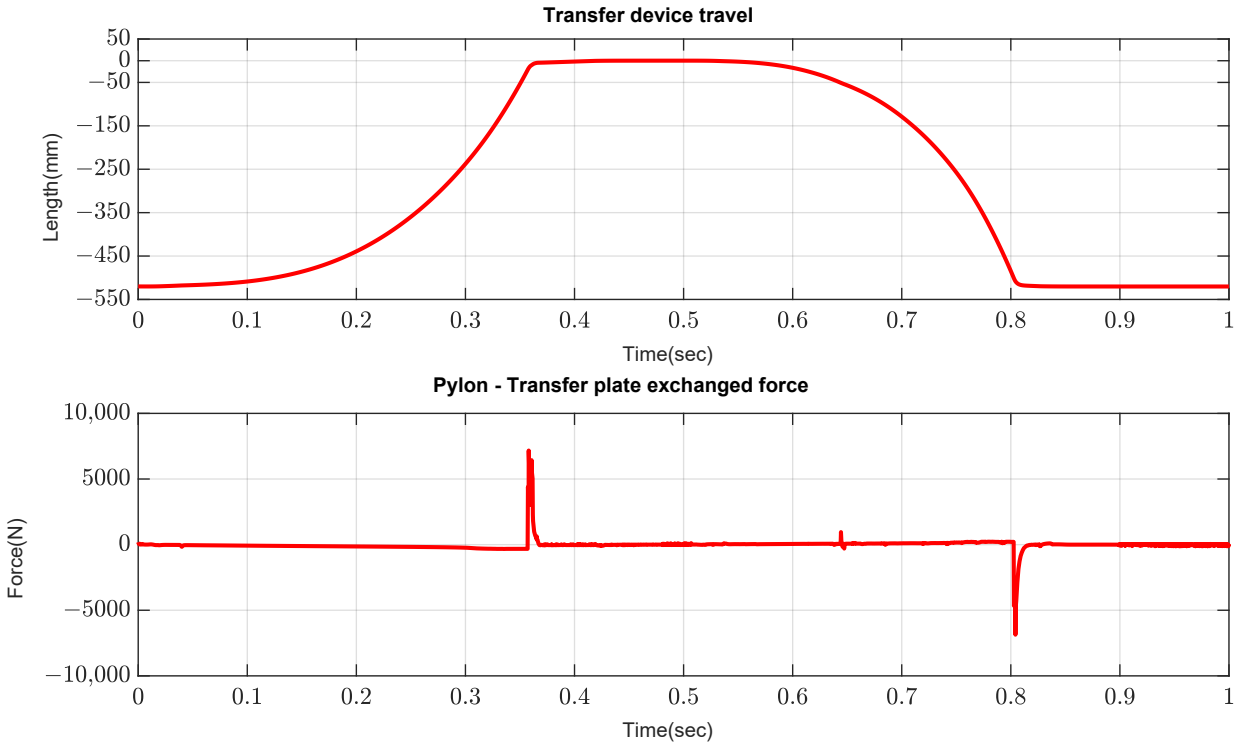

Figure 8. Transfer plate travel and load on the pylon during the motion.

The peak forces obtained during the evacuation and grasping phases are 7170 N and −6860 N, respectively.

5. Optimization

A preliminary structural analysis on the pylon subjected to the impulsive forces of the two load cases is carried out, to evaluate if there is the opportunity to apply the TO at the component. In the current design status, the material chosen for the production of this component is structural steel C45E; its mechanical properties are shown in Table 3.

Table 3. Mechanical properties of C45E.

Property	Value
Density (kg/m^3)	7850
Elastic modulus (GPa)	200
Poisson's ratio	0.29
Yield strength (MPa)	450
Tensile strength (MPa)	585

The constraint conditions are set coherently with the functioning of the device. In the FEM model are also included the end stop reference and the rail guide, in order to apply a constraint condition similar to that of the real system. The resultant constraint conditions and loads applied to the pylon are shown in Figure 9.

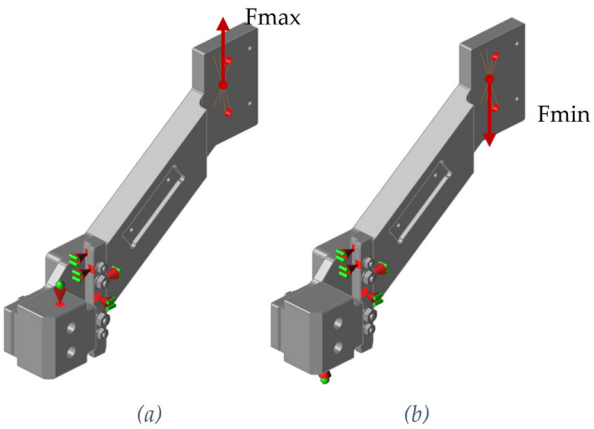

Figure 9. Constraint condition for the maximum force load case (**a**). Constraint condition for the minimum force load case (**b**).

In Figure 10, the results of the FEM structural analysis highlight that the maximum stress on the pylon is located at the interface between the pylon and the rail guide for both of the load cases analyzed, with a maximum of 253 MPa for the worst case scenario of the maximum force (end of evacuation phase), with a minimum safety factor of 1.77.

The results of the FE analysis also show that most of the pylon is lightly loaded, leaving room to optimize the geometry with a mass minimization focus.

A two-iteration approach is adopted to first quickly assess the potential performance gains and then to refine the design for practical manufacturing.

The goal of the first iteration is to rapidly evaluate the effectiveness of the proposed simulation-optimization workflow. The raw STL result from the TO is converted into a CAD file with only minor changes. This makes it possible to feed the optimized geometry back into the multibody model immediately, allowing for a swift verification of the potential reduction in cycle time without investing significant effort in CAD cleanup and manufacturability refinement.

The second iteration is performed to create a practical, robust, and manufacturable component based on the insights from the first attempt. To address the geometric issues of the first iteration, the design space for the TO is simplified, particularly around bolt

connection joints, to prevent the formation of critical geometries. The resulting raw TO geometry is then carefully interpreted into a final CAD model using the polyNURBS tool. This DfAM step involved smoothing surfaces, filleting sharp edges to reduce stress concentrations, and ensuring continuous and appropriately thick sections to guarantee it could be successfully produced via PBF-LB.

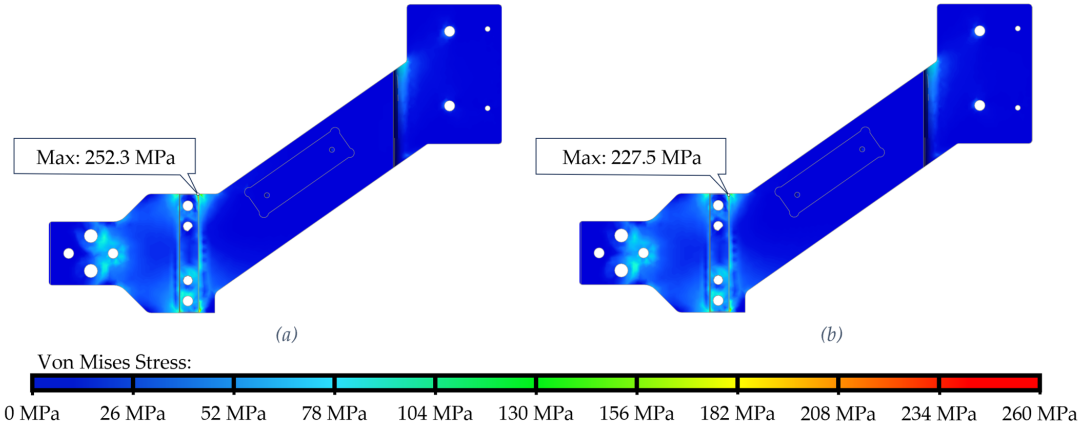

Figure 10. Von Mises equivalent stress for (**a**) max force load case and (**b**) min force load case.

5.1. Topology Optimization—First Iteration

With the knowledge of the load requirements and functionality of the pylon, the element is now being redesigned applying the Design for Additive Manufacturing (DfAM) approach as illustrated in Figure 1 [20].

The first steps of the DfAM process include defining the load cases, boundary conditions, material properties, and the available design space. The load conditions are defined by multibody simulation, and the remaining part of the process is carried out using the Inspire-Optistruct software. The design space is defined taking into account the free space available in the press area.

To accurately describe the constrained condition of the pylon, the prismatic rail guide is also incorporated. The rail guide is rigidly connected to the pylon and is constrained using a linear constraint. Furthermore, a constraint is added to simulate the interaction between the end stop and the shock absorber. The shock absorber operates as a spring-damper system during the dynamic operation of the device. However, in the TO process, the shock absorber is modeled as a fixed element in the FEM static analysis. Figure 11 shows the constrained system. The pylon experiences two load conditions during operation: one at the end of the grasping phase and another at the end of the evacuation phase. The Inspire software enables the setting of two load conditions. The first load has a force level of F = −6860 N, while the second load has a force level of F = 7170 N. Although the constraint condition changes between the two load conditions in terms of the direction of the rail constraint associated with the shock absorber, the constraint type remains the same. The contacts between the parts are set coherently with the real connection existing between them.

The analysis considers two different material solutions for building the pylon. The materials considered are compatible with the DPBF 3D printing machine EOS M290, available in the laboratories of the Department of Production Engineering (DIGEP) of Politecnico di Torino. The chosen materials are listed in Table 4. The properties refer to the material after the heat treatment.

The model in Figure 11 is used with the TO tool built into the Inspire 2022.2 software. The topology optimizer is set with both the load cases and the maximum element size.

The criterion for the TO analysis is mass minimization, applying a safety factor of 2 for stress analysis.

Table 4. Mechanical properties of the chosen materials.

Parameter	EOS AL2139 AM [41]	EOS Maraging Steel MS1 (1.2709) [42]
Yield Strength (MPa)	460	2000
Tensile Strength (MPa)	520	2080
Elongation at Break (%)	6	4

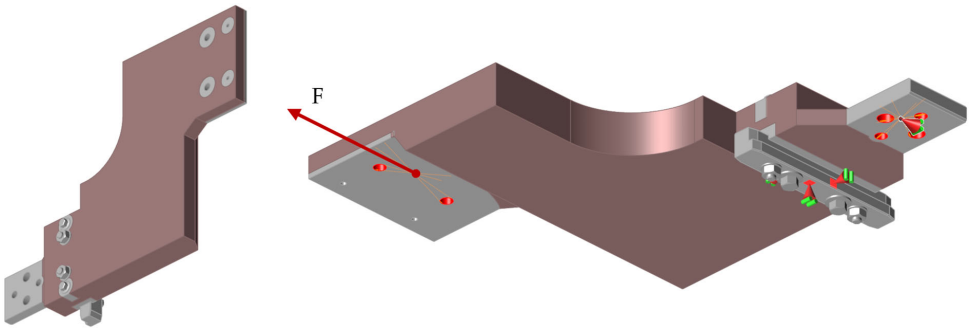

Figure 11. Design space of the pylon as input for the TO, constraint conditions, and load application. (**a**) F = −6860 N, (**b**) F = 7170 N. The design space is represented in brown, the non-design space is represented in grey.

To systematically redesign the component, a formal topology optimization problem is defined and solved using the Inspire-Optistruct software.

The optimization problem is formulated to achieve the primary goal of improving the device's dynamic performance by reducing its moving mass. This is structured as follows:

- Objective Function: Minimize the mass of the component.
- Constraint: The maximum Von Mises stress within the component must not exceed the material's allowable stress. A safety factor of 2 is applied to the material's yield strength, ensuring the final design's structural integrity and reliability under the dynamic loads.
- Load Cases: The two peak load cases (grasping and evacuation phases) identified in the multibody simulation are applied in the optimization setup to ensure that the geometry is robust for all critical operating conditions.

The principle of topology optimization is to find the most efficient distribution of a limited amount of material within a defined design space to sustain a given set of loads. The solver quantifies this by using the gradient-based method, SIMP—Solid Isotropic Material with Penalization–within the Optistruct suite, that iteratively removes material from regions of low stress and retains it in regions of high stress. This process creates an ideal load path, effectively maximizing stiffness for a given mass, or in this case, minimizing mass while satisfying the stress constraint.

The underlying structural analyses are conducted using the Optistruct solver. The design space is discretized using a 3D solid tetrahedral mesh. A linear static analysis is performed for each of the two peak load cases. The software solves the fundamental equations of static equilibrium to determine the displacement and stress fields throughout the component for each load case. These stress results are then used by the optimizer in each iteration to guide the material removal process.

The first-attempt STL results of the TO process for both the materials is converted into a CAD file with minor changes. This is because the intention of the proposed method is to

evaluate immediately the performance of the optimized geometry prior to the geometry cleaning for the AM process needed for a production piece. This step allows the designer to verify the effectiveness of the study without refining the CAD geometry, making it possible to immediately evaluate each result in the redesign process.

The first results of the TO are shown in Figure 12. The resulting geometries have some clear issues such as indentation, section striction and imperfections, due to the simple transposition of the STL result in the parametric CAD file. However, the geometry is used to evaluate the performances using the developed multibody model. If the results are promising, a second iteration is carried out to define a geometry that could be produced. The obtained masses of the pylon for the two results are 426 g for the EOS AL2139 AM and 1006 g for the EOS MS1, with a 16.4% reduction of the total mass of the transfer device.

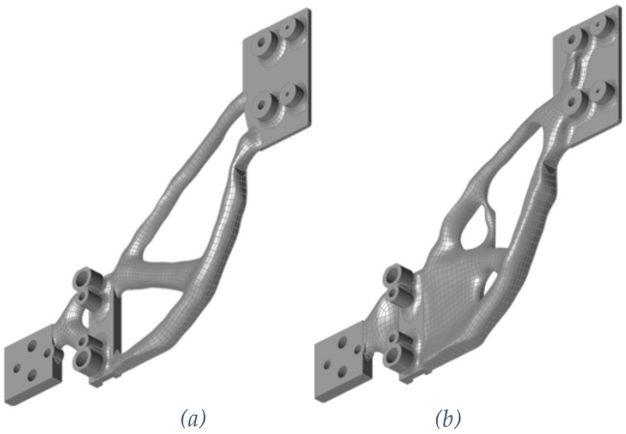

Figure 12. First-attempt TO results: (**a**) EOS MS1, (**b**) EOS AL2139.

The obtained TO geometries are introduced in the multibody model to verify the performance of the improved system. The results are immediately available due the integrated simulation process proposed.

In Figure 13, the product evacuation phase of the device is compared between the original geometry and the TO geometry for both cases. The end of the evacuation phase, which makes it possible to evaluate the improvement in terms of process cycle time with the TO components, is detailed in Figure 14.

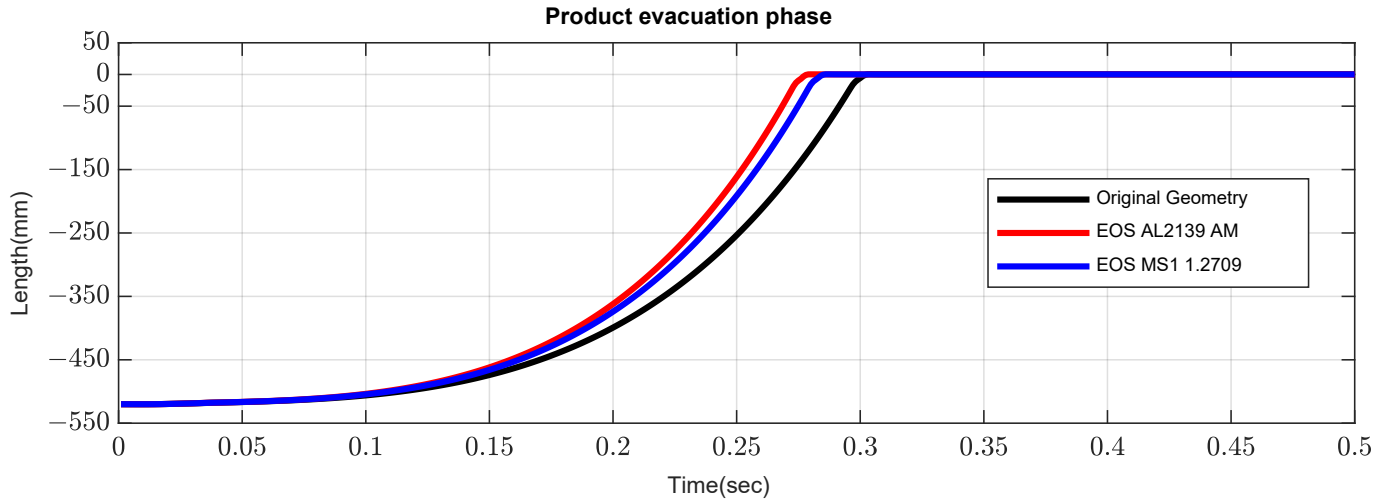

Figure 13. Impact of the optimized geometries on the performance of the device during the evacuation phase.

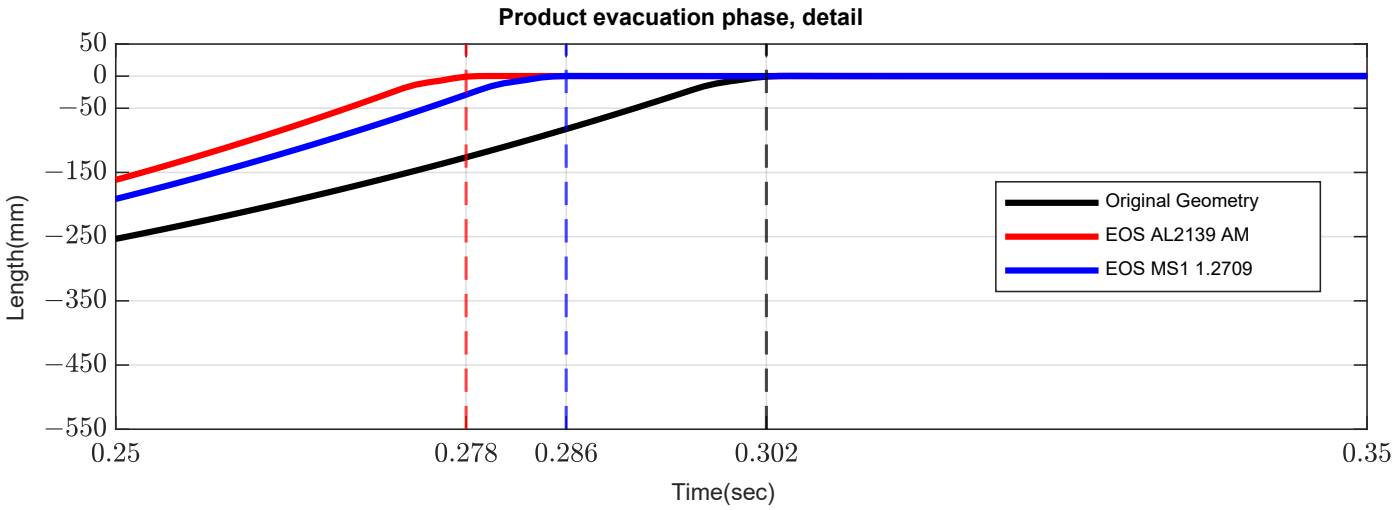

Figure 14. Detail of the end of the evacuation phase.

The increase in performance is larger in the grasping translation phase (Figure 15), when the product is not involved in the movement and the device moves only its components, with a minor total weight. The working cycle of the transfer device involves the evacuation phase, a stop of 0.2 s, and the product grasping phase. The detail of the translating time is shown in Figure 16.

The total improvement of performance using the TO parts is summarized in Table 5.

Table 5. Performance comparison, first attempt geometries.

Geometry	Translation Phase Duration (s)	Time Reduction (%)
C45E Geometry—baseline	0.763	0%
EOS MS1 1.2709 Geometry	0.723	5.2%
EOS Al2139 AM Geometry	0.706	7.5%

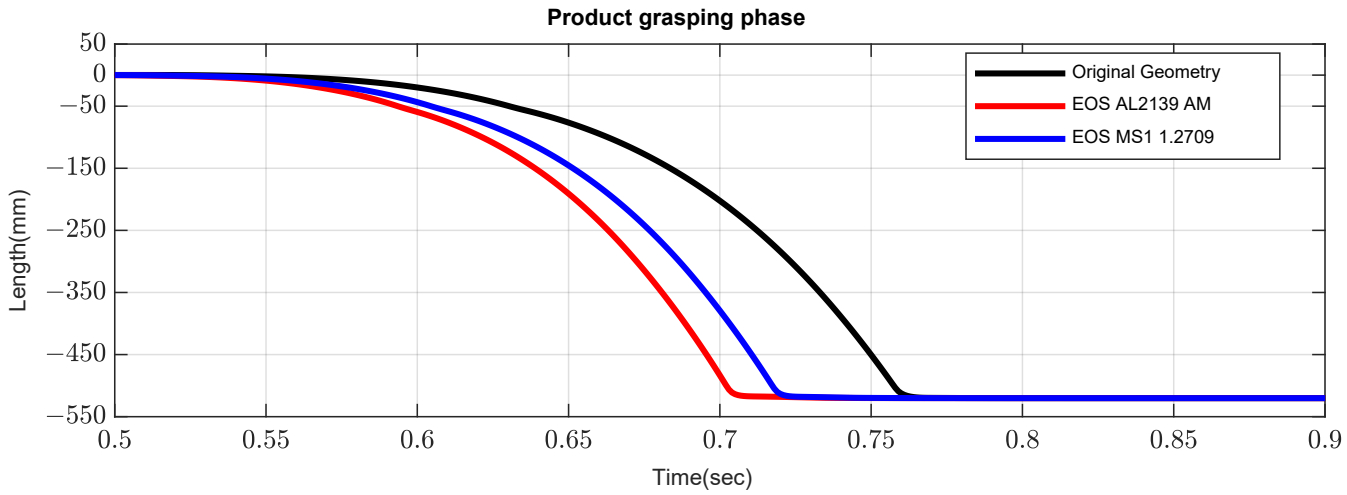

Figure 15. Impact of the optimized geometries on the performance of the device during the grasping phase.

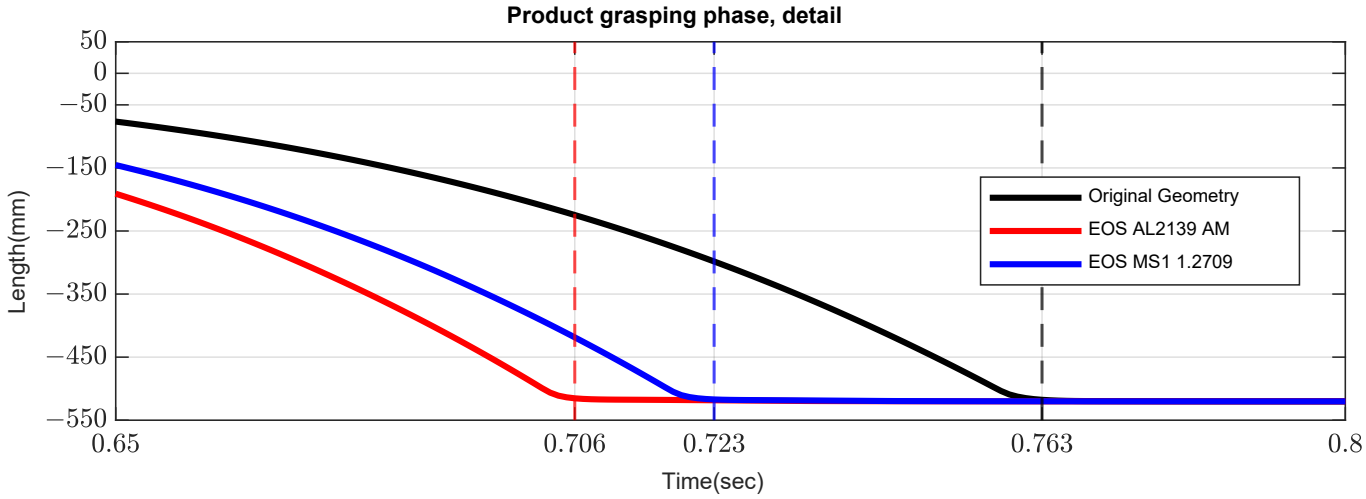

Figure 16. Detail of the performance improvement in terms of translation time of the product grasping phase.

5.2. Topology Optimization—DfAM Solution

The second iteration started with another TO; a more simplified geometry for the design space is used to avoid the critical geometries of the bolt connection joints. Figure 17a shows the design space as input for the TO. TO results are shown in Figure 17b,c.

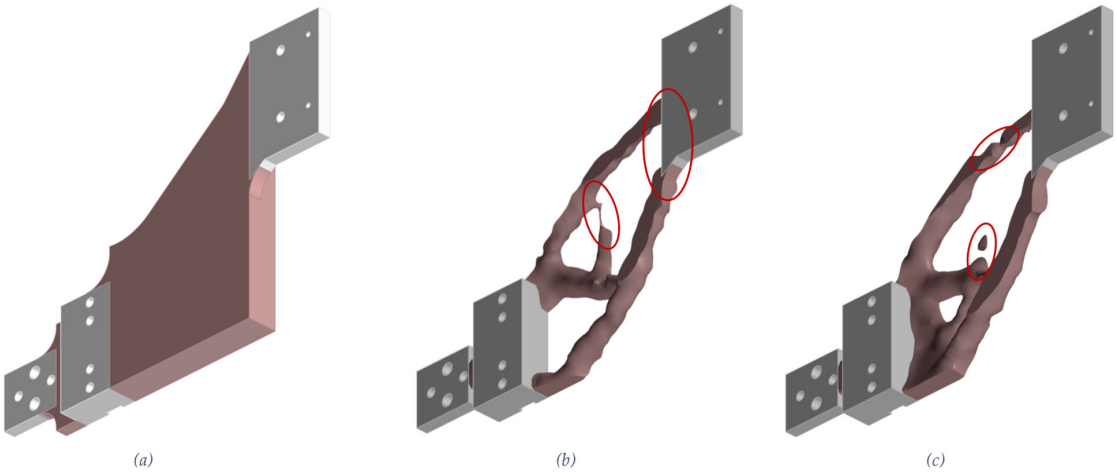

Figure 17. Design space of the pylon for the second iteration TO study (**a**); TO results for the material EOS MS1 1.2709 (**b**) and for the material EOS Al2139 AM (**c**).

Still, both the materials are considered for this second iteration. Figure 18 shows the results of the TO of the pylon for both the materials, EOS MS1 1.2709 and EOS AL2139 AM. The main problems, similar for both the results, are highlighted: The slenderness of some structural parts and the uneven compliance between the optimized volume with the rest of the component can be seen.

Both geometries are interpreted in CAD format using the polyNURBS tool built into the Inspire software. The problems are corrected to obtain a continuous geometry that can be produced. Sharp edges are filleted, as well as the junctions between TO parts and the rest of the component. The final geometries are shown in Figure 18. The final mass of the resulting parts is 1336 g for the EOS MS1 (Figure 18a) and 538 g for the EOS AL2139 (Figure 18b). The increase in mass is significant with respect to the first iteration, and this is due to the definition of a geometry that can be efficiently manufactured.

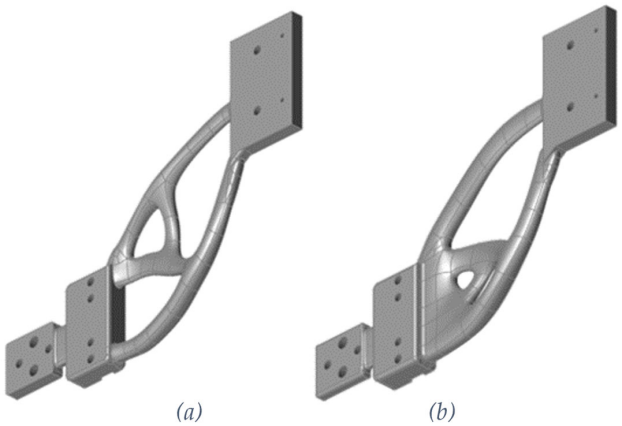

Figure 18. Final pylon results: EOS MS1 material (**a**), EOS AL2139 material (**b**).

5.3. FE Analysis

The optimized geometries are verified through FE analysis. This is a key step in the redesign for additive manufacturing process to verify that the CAD interpretation of the TO is effectively strong enough for the application. The Inspire software interface is used to solve the structural FE analysis using the Optistruct solver. The results in Figure 19 show that the maximum stress for both the components is below the Rp_{02} limit of the heat-treated material. This results in a minimum safety factor of 2 for both solutions.

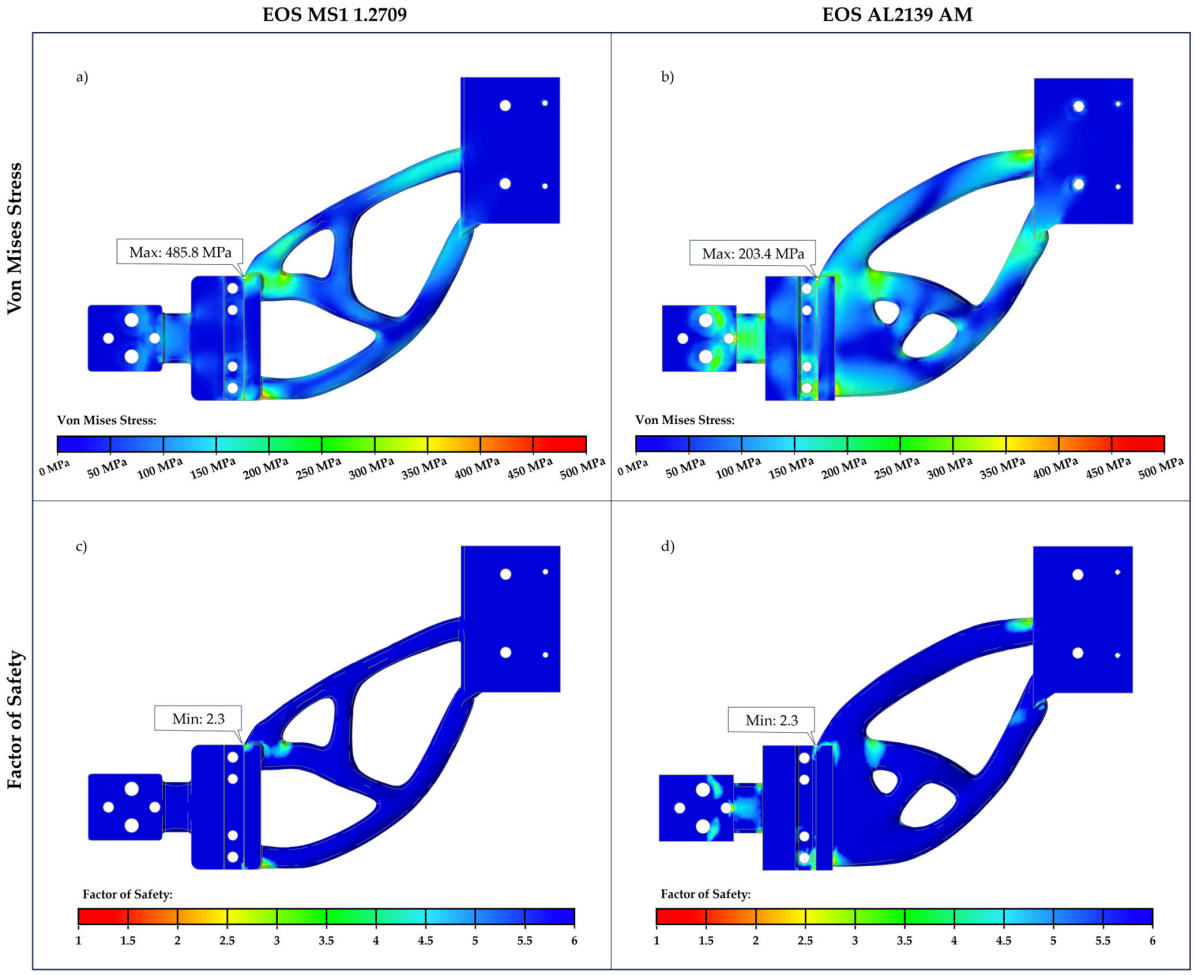

Figure 19. FEM analysis results of the final geometry for both the materials: Von Mises Stress for EOS MS1 material (**a**) and EOS Al1 material (**b**), safety factor for EOS MS1 material (**c**) and EOS Al1 material (**d**).

The obtained final geometry is then verified again using the multibody tool developed, to verify the effectiveness of the process improvement, even with the increased weight due to manufacturing constraints. The transfer device work cycle comparison is shown in Figure 20.

In Figure 21, the detail of the end time of the working cycle shows a sensible reduction in terms of the working cycle, even with the increased mass due to the CAD interpretation process. Quantitative results are summarized in Table 6.

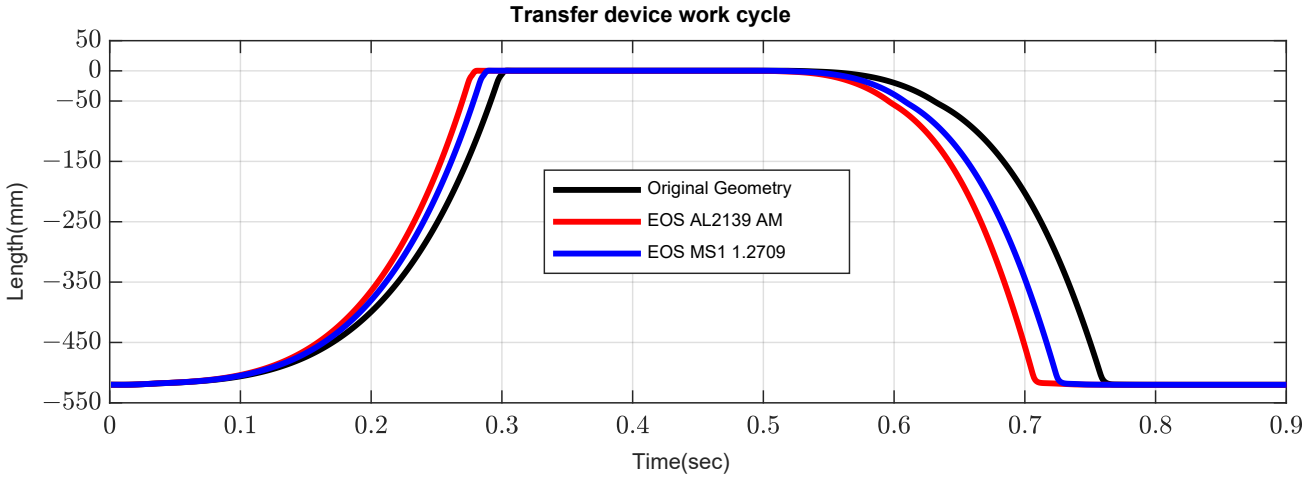

Figure 20. Comparison of the transfer device work cycle with the different geometries.

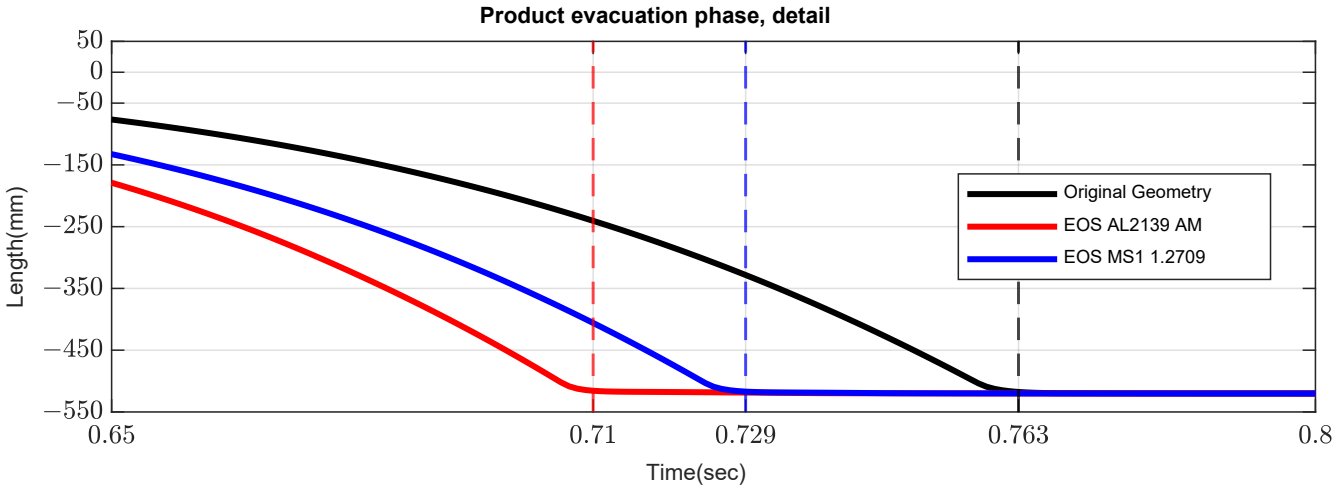

Figure 21. Detail of the end time of the device work cycle; comparison between the three geometries.

Table 6. Performance comparison, final geometries.

Geometry	Translation Phase Duration (s)	Time Reduction (%)
C45E Geometry	0.763	0%
EOS MS1 1.2709 Geometry	0.729	4.5%
EOS Al2139 AM Geometry	0.710	6.9%

6. Cost Analysis

Manufacturing costs of AM-produced parts depends on several factors [43], such as the type of process, the material costs, the labor costs, the volume of the component, and the machine operating cost. The model proposed in [44] and further developed in [45,46] is used in this work to estimate the costs for the PBF-LB production of the redesigned pylon. The

parameters necessary for the calculations are extracted from the AM data sheets and from a study by Roland Berger [47]. Some key parameters, such as the processing time and the numbers of parts produced per job, are calculated using Autodesk Netfabb 2025.0 software. The cost analysis is performed for the resulting geometries of both EOS materials. However, the geometry to be produced by PBF-LB is simplified by removing the screw holes, which will be later drilled in the post-processing phase.

It is assumed that the PBF-LB machine volume is used to produce the pair of brackets simultaneously, to maximize the efficiency of the machine.

The different scenarios of orientation of the part in the building volume are shown in Figure 22. The parameters evaluated for the choice of each scenario are the support volume, the build height, and the build time. The EOS MS1 1.2709 solution minimizes the support volume in the first scenario; however, the third scenario minimizes the build time, which is the condition of minimizing the production cost. The third scenario is also chosen for the EOS AL2139 AM solution, since it is the most economically convenient. The chosen orientation of the third scenario allows maintaining the datum feature for the support removal operation in the post-processing phase.

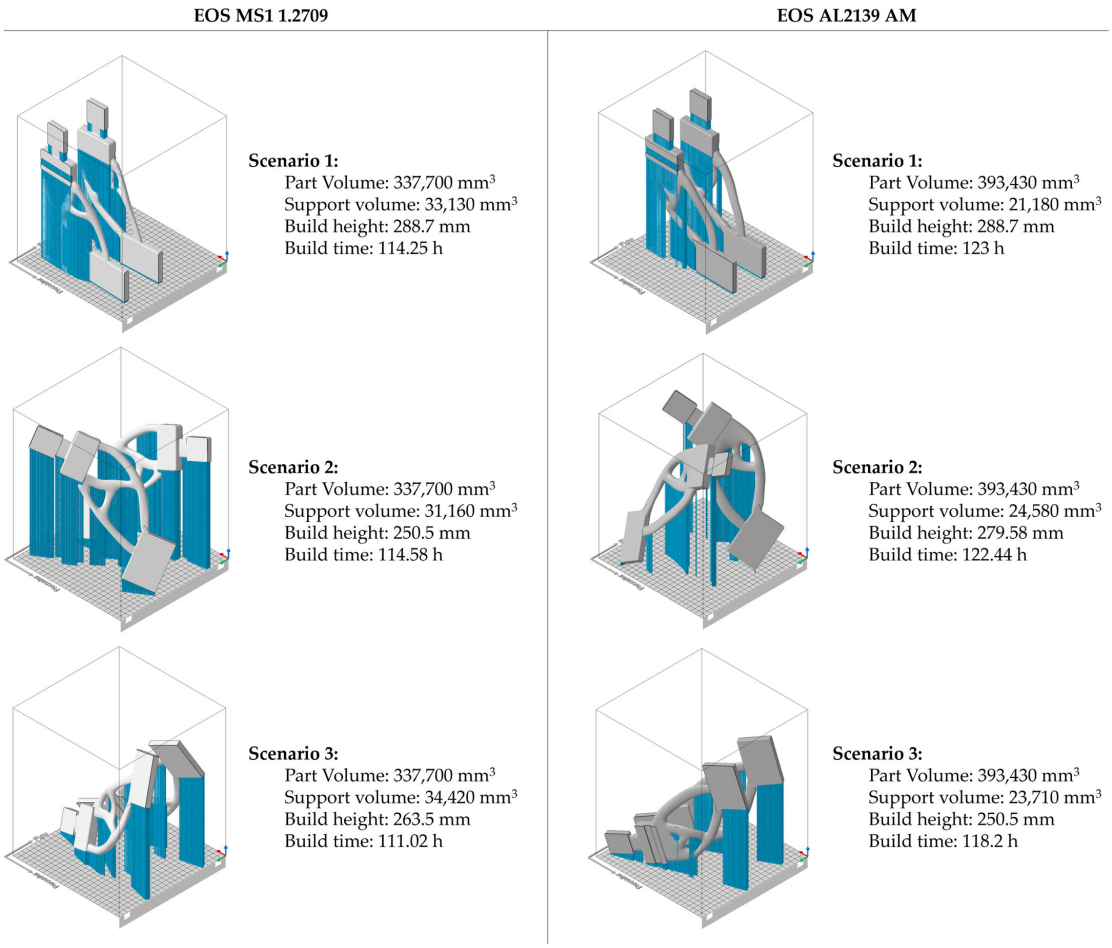

Figure 22. Part orientation scenarios for PBF-LB production of the redesigned pylon of the two EOS MS1 and EOS AL2129 materials.

The manufacturing cost per part P is dependent on the material cost M_{AM} and the production cost P_{AM}, which is dependent by the processing cost, the post-processing cost, the heat treatment cost, and the human work cost [46]:

$$c_{AM} = (M_{AM} + P_{AM}) \tag{2}$$

The material cost per part M_{AM}, the material cost M in EUR/kg, the part volume V, and the sintered material density D. A coefficient of 1.1 is applied to account for additional material amount considering support volume and powder losses during the process [44]:

$$M_{AM} = M \cdot V \cdot D \cdot 1.1 \quad (3)$$

The production cost is equal to the sum of the pre-processing cost A_P, the processing cost C_P, and the post-processing cost B_P:

$$P_{AM} = A_P + C_P + B_P \quad (4)$$

The pre-processing cost per part depends on the number of parts per job N, the labor cost O, and the set-up time per build A:

$$A_P = O \cdot A / N \quad (5)$$

The processing cost per part C_P depends on the machine cost per hour CH, the build time T, and the number of parts per job:

$$C_P = T \cdot CH / N \quad (6)$$

The post-processing cost per part B_P depends on the CNC machining cost for support removal and polishing PM and the heat treatment cost per part HT:

$$B_P = PM + HT \quad (7)$$

In the post-processing phase, machining is needed to remove the support structures and to finish the part surface. In the PBF-LB pylon, the screw holes should also be drilled because they were removed from the redesigned geometry for AM production purposes. The machining cost depends on the labor cost for part positioning and the CNC machine cost, which depends on the operation time. The setup time has been estimated at 72 min per job [46]; the machining time has been estimated assuming a cutting speed of 1 m/min. The total machining time is estimated on the basis of the supported area, the passes needed, and the drilling time.

The heat treatment cost depends on the labor cost, the energy cost, the furnace used, and the heat treatment phases described by the material supplier. For the case study, a 9 kW furnace is considered with a utilization factor of 60%. The EOS MS1 needs an 8 h heat treatment in the furnace, whereas the EOS AL2139 needs 45 min of heat treatment in the furnace and 3 days of aging at room temperature. The energy cost is assumed from the average value of the cost of electricity on the Italian market in 2023.

The results of the cost analysis are reported in Table 7 for the AL2139 pylon, and in Table 8 for the MS1 pylon.

Table 7. Total cost per structural pylon of EOS AL2139 AM.

Parameter	Symbol	Value	Unit	Source
Number of parts produced per job	N	2		
Material cost per kg	M	152	EUR/kg	
Part volume	V_P	196,715	mm^3	
Support volume (per part)	V_S	118,55	mm^3	
Density of the sintered material	D	2.7×10^{-3}	g/mm^3	
Mass of material per part	$U = V \cdot D$	0.56	kg	
Material cost per part	M_{AM}	85.60	EUR	

Table 7. *Cont.*

Parameter	Symbol	Value	Unit	Source
Machine operator cost per hour	O	50	EUR/h	[46]
Set-up time per build	A	0.5	h	[47]
Pre-processing cost per part	$A_P = O{\cdot}A/N$	12.5	EUR	
Machine cost per hour	CH	44	EUR/h	[46]
Build time	T	118.2	h	
Machine cost per build	$T{\cdot}CH$	5200.8	EUR	
Processing cost per part	$C_P = T{\cdot}CH/N$	2600.4	EUR	
Machine operator cost per hour	O	50	EUR/h	[46]
CNC machine cost per hour	CC	60	EUR/h	[45]
CNC machining time per part	t_{CNC}	0.21	h	
CNC setup time per part	t_{CS}	0.6	h	[46]
CNC machining cost per part	$PM = O{\cdot}t_{CS} + CC{\cdot}t_{CNC}$	42.64	EUR	
Heat treatment set-up time per part	t_{ST}	0.5	h	
Heat treatment energy consumption per part	E_{HT}	2.03	kWh	
Heat treatment duration	t_{HT}	0.75	h	
Energy cost	e_{EC}	0.127	EUR/kWh	
Heat treatment cost per build	$HT = E_{HT}{\cdot}e_{EC}{\cdot}t_{HT} + t_{ST}{\cdot}O$	20.26	EUR	
Post-processing cost per part	$B_P = PM + HT$	62.9	EUR	
Manufacturing cost per part	$P_{AM} = M_{AM} + A_P + C_P + B_P$	**2761.39**	EUR	

Table 8. Total cost per structural pylon of EOS MS1 1.2709.

Parameter	Symbol	Value	Unit	Source
Number of parts produced per job	N	2		
Material cost per kg	M	193	EUR/kg	
Part volume	V_P	168,850	mm^3	
Support volume (per part)	V_S	17,210	mm^3	
Density of the sintered material	D	8.1×10^{-3}	g/mm^3	
Mass of material per part	$U = V{\cdot}D$	1.51	kg	
Material cost per part	M_{AM}	390.87	EUR	
Machine operator cost per hour	O	50	EUR/h	[46]
Set-up time per build	A	0.5	h	[47]
Pre-processing cost per part	$A_P = O{\cdot}A/N$	12.5	EUR	
Machine cost per hour	CH	44	EUR/h	[46]
Build time	T	111.02	h	
Machine cost per build	$T{\cdot}CH$	4884.88	€	
Processing cost per part	$C_P = T{\cdot}CH/N$	2442.44	€	
Machine operator cost per hour	O	50	EUR/h	[46]
CNC machine cost per hour	CC	60	EUR/h	[45]
CNC machining time per part	t_{CNC}	0.22	h	
CNC setup time per part	t_{CS}	0.6	h	[46]
CNC machining cost per part	$PM = O{\cdot}t_{CS} + CC{\cdot}t_{CNC}$	43.16	EUR	
Heat treatment set-up time per part	t_{ST}	0.5	h	
Heat treatment energy consumption per part	E_{HT}	21.6	kWh	
Heat treatment duration	t_{HT}	8	h	
Energy cost	e_{EC}	0.127	EUR/kWh	
Heat treatment cost per build	$HT = E_{HT}{\cdot}e_{EC}{\cdot}t_{HT} + t_{ST}{\cdot}O$	22.60	EUR	
Post-processing cost per part	$B_P = PM + HT$	65.76	EUR	
Manufacturing cost per part	$P_{AM} = M_{AM} + A_P + C_P + B_P$	**2811.57**	EUR	

The cost analysis shows that there is no significant difference between the two solutions and materials in terms of manufacturing costs. Therefore, the driving factor for the best solution is the desired effect, which leads to the choice of the EOS AL2139 AM material. However, the estimated cost for traditional manufacturing the single pylon by CNC machining is around EUR 400. This value is based on the quote provided by the original supplier of the machined components. Hence, the AM pylon is about 5 times more

expensive than the traditional part. However, the final choice of the manufacturing process for this case study is driven by multiple factors, including the impact of the pylon cost on the whole die cost, which is to be evaluated separately, as it includes multiple components that are still under development.

7. Conclusions

This study discusses the redesign and optimization of a load-bearing pylon used in a device to evacuate products in a fine blanking plant. The redesign is proposed to optimize the pylon mass in order to improve the performance of the device and the process time. To evaluate the dynamic load conditions of the pylon, a multibody model of the device is developed, which includes the actuation elements, the damping behavior of the end stops, and contact mechanics. The results of the dynamic analysis are used as inputs in the redesign for additive manufacturing process applied to the pylon.

So, the work proposes a method to integrate dynamic analysis performed using multibody modeling techniques in the redesign for additive manufacturing process, highlighting is the power of the possibility to evaluate the desired effect and the reduction in process time, prior to the manufacturing of a prototype. Different solutions are proposed and compared for EOS MS1 1.2709 and EOS AL2139 AM. The performed analyses show how the capabilities of the device can be increased up to 6.9% for the EOS AL2139 AM geometry.

The cost analysis highlights that the two solutions developed for AM are equivalent in terms of costs, so the chosen geometry is the AL2139 AM solution, since it leads to higher performance of the devices. A final choice between PBF-LB and the traditional technique, which is cheaper, cannot be made at this stage, as the design process for the other components of the whole die is still under development. However, it can be asserted that the AM solution is to be chosen when its reduction in process time leads to an increase in productivity which is higher than the increased cost of the die due to the introduction of AM parts. The cost-effectiveness of the AM solution arises when its impact on the press working cycle is relevant even considering downtimes, such as the set-up time and the supply material change time, which can be relevant for the case study proposed here. However, a more precise estimation is not possible at this stage of the design process.

Author Contributions: Conceptualization, S.M., P.M. and D.S.; methodology, D.S., P.M. and S.M.; software, D.S.; validation, D.S.; formal analysis, D.S.; investigation, D.S.; resources, P.M. and S.M.; data curation, D.S.; writing—original draft preparation, D.S.; writing—review and editing, P.M. and S.M.; visualization, D.S.; supervision, P.M. and S.M.; project administration, P.M. and S.M. All authors have read and agreed to the published version of the manuscript.

Funding: This research received no external funding.

Data Availability Statement: The original contributions presented in this study are included in the article. Further inquiries can be directed to the corresponding author.

Acknowledgments: The authors thank Util Industries SpA for supporting this research.

Conflicts of Interest: The authors declare no conflicts of interest.

References

1. Campbell, I.; Bourell, D.; Gibson, I. Additive Manufacturing: Rapid Prototyping Comes of Age. *Rapid Prototyp. J.* **2012**, *18*, 255–258. [CrossRef]
2. Hitzler, L.; Merkel, M.; Hall, W.; Öchsner, A. A Review of Metal Fabricated with Laser- and Powder-Bed Based Additive Manufacturing Techniques: Process, Nomenclature, Materials, Achievable Properties, and Its Utilization in the Medical Sector. *Adv. Eng. Mater.* **2018**, *20*, 1700658. [CrossRef]

3. Alami, A.H.; Olabi, A.G.; Alashkar, A.; Alasad, S.; Aljaghoub, H.; Rezk, H.; Abdelkareem, M.A. Additive Manufacturing in the Aerospace and Automotive Industries: Recent Trends and Role in Achieving Sustainable Development Goals. *Ain Shams Eng. J.* **2023**, *14*, 102516. [CrossRef]
4. Singh, S.; Mehla, S.; Bhargava, S.K.; Ramakrishna, S. History and Evolution of Additive Manufacturing. In *Additive Manufacturing for Chemical Sciences and Engineering*; Springer Nature: Singapore, 2022; pp. 19–51.
5. DebRoy, T.; Wei, H.L.; Zuback, J.S.; Mukherjee, T.; Elmer, J.W.; Milewski, J.O.; Beese, A.M.; Wilson-Heid, A.; De, A.; Zhang, W. Additive Manufacturing of Metallic Components–Process, Structure and Properties. *Prog. Mater. Sci.* **2018**, *92*, 112–224. [CrossRef]
6. De Leon, E.; Riensche, A.; Bevans, B.D.; Billings, C.; Siddique, Z.; Liu, Y. A Review of Modeling, Simulation, and Process Qualification of Additively Manufactured Metal Components via the Laser Powder Bed Fusion Method. *J. Manuf. Mater. Process.* **2025**, *9*, 22. [CrossRef]
7. du Plessis, A. Effects of Process Parameters on Porosity in Laser Powder Bed Fusion Revealed by X-Ray Tomogra-phy. *Addit. Manuf.* **2019**, *30*, 100871. [CrossRef]
8. Sing, S.L.; Yeong, W.Y. Laser Powder Bed Fusion for Metal Additive Manufacturing: Perspectives on Recent Developments. *Virtual Phys. Prototyp.* **2020**, *15*, 359–370. [CrossRef]
9. Seede, R.; Zhang, B.; Whitt, A.; Picak, S.; Gibbons, S.; Flater, P.; Elwany, A.; Arroyave, R.; Karaman, I. Effect of Heat Treatments on the Microstructure and Mechanical Properties of an Ultra-High Strength Martensitic Steel Fabricated via Laser Powder Bed Fusion Additive Manufacturing. *Addit. Manuf.* **2021**, *47*, 102255. [CrossRef]
10. Fiocchi, J.; Tuissi, A.; Biffi, C. Heat Treatment of Aluminium Alloys Produced by Laser Powder Bed Fusion: A Review. *Mater. Des.* **2021**, *204*, 109651. [CrossRef]
11. Aghajani, S.; Wu, C.; Li, Q.; Fang, J. Additively Manufactured Composite Lattices: A State-of-the-Art Review on Fabrica-tions, Architectures, Constituent Materials, Mechanical Properties, and Future Direc-tions. *Thin-Walled Struct.* **2023**, *197*, 111539. [CrossRef]
12. Souza, J.; Großmann, A.; Mittelstedt, C. Micromechanical Analysis of the Effective Properties of Lattice Structures in Additive Manufacturing. *Addit. Manuf.* **2018**, *23*, 53–69. [CrossRef]
13. Zhuang, J.; Zeng, F. Research and Experimental Verification of an Efficient Subframe Lightweighting Method Integrating SIMP Topology and Size Optimization. *Appl. Sci.* **2025**, *15*, 8192. [CrossRef]
14. Sun, J.; Tian, Q.; Hu, H.; Pedersen, N.L. Topology Optimization of a Flexible Multibody System with Variable-Length Bodies Described by ALE–ANCF. *Nonlinear Dyn.* **2018**, *93*, 413–441. [CrossRef]
15. Murat, F.; Kaymaz, I.; Şensoy, A.T. Reliability-Based Topology Optimization Considering Overhang Constraints for Additive Manufacturing Design. *Appl. Sci.* **2025**, *15*, 6250. [CrossRef]
16. Prathyusha, A.; Babu, G.R. A Review on Additive Manufacturing and Topology Optimization Process for Weight Reduction Studies in Various Industrial Applications. *Mater. Today Proc.* **2022**, *62*, 109–117. [CrossRef]
17. Alfaify, A.; Saleh, M.; Abdullah, F.; Al-Ahmari, A. Design for Additive Manufacturing: A Systematic Review. *Sustainability* **2020**, *12*, 7936. [CrossRef]
18. Obi, M.U.; Pradel, P.; Sinclair, M.; Bibb, R. A Bibliometric Analysis of Research in Design for Additive Manufacturing. *Rapid Prototyp. J.* **2022**, *28*, 967–987. [CrossRef]
19. Egan, P.F. Design for Additive Manufacturing: Recent Innovations and Future Directions. *Designs* **2023**, *7*, 83. [CrossRef]
20. Emmelmann, C.; Sander, P.; Kranz, J.; Wycisk, E. Laser Additive Manufacturing and Bionics: Redefining Lightweight Design. *Phys. Procedia* **2011**, *12*, 364–368. [CrossRef]
21. Großmann, A.; Weis, P.; Clemen, C.; Mittelstedt, C. Optimization and Re-Design of a Metallic Riveting Tool for Additive Manufacturing—A Case Study. *Addit. Manuf.* **2020**, *31*, 100892. [CrossRef]
22. Salmi, A.; Vecchi, G.; Atzeni, E.; Iuliano, L. Hybrid Multi-Criteria Decision Making for Additive or Conventional Process Selection in the Preliminary Design Phase. *Designs* **2024**, *8*, 110. [CrossRef]
23. Aljabali, B.A.; Parupelli, S.K.; Desai, S. Generalized Design for Additive Manufacturing (DfAM) Expert System Using Compliance and Design Rules. *Machines* **2025**, *13*, 29. [CrossRef]
24. Kang, B.-S.; Park, G.-J.; Arora, J.S. A Review of Optimization of Structures Subjected to Transient Loads. *Struct. Multidiscip. Optim.* **2006**, *31*, 81–95. [CrossRef]
25. Samin, J.C.; Brüls, O.; Collard, J.F.; Sass, L.; Fisette, P. Multiphysics Modeling and Optimization of Mechatronic Multibody Systems. *Multibody Syst. Dyn.* **2007**, *18*, 345–373. [CrossRef]
26. Raviola, A.; Guida, R.; Bertolino, A.C.; De Martin, A.; Mauro, S.; Sorli, M. A Comprehensive Multibody Model of a Collaborative Robot to Support Model-Based Health Management. *Robotics* **2023**, *12*, 71. [CrossRef]
27. Bertolino, A.C.; De Martin, A.; Guida, R.; Sorli, M. Adams multibody simulation of jamming in the recirculation channel of a single-nut ball screw. In Proceedings of the ASME 2023 International Mechanical Engineering Congress and Exposition, New Orleans, LA, USA, 29 October–2 November 2023.

28. Guerrero, D.A.; Jacobs, G.; Zerwas, T.; Delgadillo, A. Integrating Topology Optimization into Model-Based Systems Engineering for Lightweight Structural Design. *Forsch. Ingenieurwesen* **2025**, *89*, 63. [CrossRef]
29. Zhu, J.; Zhou, H.; Wang, C.; Zhou, L.; Yuan, S.; Zhang, W. A Review of Topology Optimization for Additive Manufacturing: Status and Challenges. *Chin. J. Aeronaut.* **2021**, *34*, 91–110. [CrossRef]
30. Bayat, M.; Zinovieva, O.; Ferrari, F.; Ayas, C.; Langelaar, M.; Spangenberg, J.; Salajeghe, R.; Poulios, K.; Mohanty, S.; Sigmund, O.; et al. Holistic Computational Design within Additive Manufacturing through Topology Optimization Combined with Multiphysics Multi-Scale Materials and Process Modelling. *Prog. Mater. Sci.* **2023**, *138*, 101129. [CrossRef]
31. Sotomayor, N.A.S.; Caiazzo, F.; Alfieri, V. Enhancing Design for Additive Manufacturing Workflow: Optimization, Design and Simulation Tools. *Appl. Sci.* **2021**, *11*, 6628. [CrossRef]
32. Rosen, D.W. Research Supporting Principles for Design for Additive Manufacturing: This Paper Provides a Comprehensive Review on Current Design Principles and Strategies for AM. *Virtual Phys. Prototyp.* **2014**, *9*, 225–232. [CrossRef]
33. Sun, J.; Tian, Q.; Hu, H. Topology Optimization of a Three-Dimensional Flexible Multibody System Via Moving Morphable Components. *J. Comput. Nonlinear Dyn.* **2018**, *13*, 021010. [CrossRef]
34. Kim, G.-W.; Park, Y.-I.; Park, K. Topology Optimization and Additive Manufacturing of Automotive Component by Coupling Kinetic and Structural Analyses. *Int. J. Automot. Technol.* **2020**, *21*, 1455–1463. [CrossRef]
35. Sorli, M.; Vigliani, A. Design Analysis of a Pneumatic Force Control Servosystem with Pressure Proportional Valve. *J. Robot. Mechatron.* **1998**, *10*, 370–376. [CrossRef]
36. Salamina, L.; Botto, D.; Mauro, S.; Pastorelli, S. Modeling of Flexible Bodies for the Study of Control in the Simulink Environment. *Appl. Sci.* **2020**, *10*, 5861. [CrossRef]
37. Zimmer Group. STANDARD ENERGY P SE 25X15 N 25 Datasheet. Available online: https://www.zimmer-group.com/fileadmin/daten/service/download-center/daempfungstechnik/dt1_industrie/damping_technology1_en.pdf#page=30.42 (accessed on 20 August 2025).
38. Adams 2020 FP1 Adams View User's Guide. 2020. Available online: https://nexus.hexagon.com/documentationcenter/zh-CH/bundle/Adams_2020_FP1_Adams_View_Command_User_Guide/resource/Adams_2020_FP1_Adams_View_Command_User_Guide.pdf (accessed on 20 August 2025).
39. Verheul, C.; ADAMS Methodology Contact Modeling. Benelux ADAMS User Meet. 2012. Available online: https://it.scribd.com/document/510700500/SayField-Verheul-ADAMS-Contacts (accessed on 20 August 2025).
40. Sapietová, A.; Gajdoš, L.; Dekýš, V.; Sapieta, M. Analysis of the Influence of Input Function Contact Parameters of the Impact Force Process in the MSC. ADAMS. In *Advances in Intelligent Systems and Computing*; Springer: Cham, Switzerland, 2016; Volume 393, pp. 243–253.
41. EOS GmbH. EOS Aluminium Al2139 AM Material Data Sheet. Available online: https://www.eos.info/it/var/assets/05-datasheet-images/Assets_MDS_Metal/EOS_Aluminium_Al2139AM/Material_DataSheet_EOS_Aluminium_Al2139%20AM_en.pdf (accessed on 20 August 2025).
42. EOS GmbH. EOS Maraging Steel MS1 Material Data Sheet. Available online: https://www.eos.info/it/var/assets/05-datasheet-images/Assets_MDS_Metal/EOS_MargingSteel_MS1/Material_DataSheet_EOS_MaragingSteel_MS1_en.pdf?v=6 (accessed on 20 August 2025).
43. Kadir, A.Z.A.; Yusof, Y.; Wahab, M.S. Additive Manufacturing Cost Estimation Models—A Classification Review. *Int. J. Adv. Manuf. Technol.* **2020**, *107*, 4033–4053. [CrossRef]
44. Atzeni, E.; Salmi, A. Economics of Additive Manufacturing for End-Usable Metal Parts. *Int. J. Adv. Manuf. Technol.* **2012**, *62*, 1147–1155. [CrossRef]
45. Atzeni, E.; Iuliano, L.; Marchiandi, G.; Minetola, P.; Salmi, A.; Bassoli, E.; Denti, L.; Gatto, A. Additive Manufacturing as a Cost-Effective Way to Produce Metal Parts. In *High Value Manufacturing: Advanced Research in Virtual and Rapid Prototyping, Proceedings of the 6th International Conference on Advanced Research and Rapid Prototyping, Leiria, Portugal, 1–5 October 2013*; CRC Press-Taylor & Francis Group: Boca Raton, FL, USA, 2014; pp. 3–8.
46. Salmi, A.; Calignano, F.; Galati, M.; Atzeni, E. An Integrated Design Methodology for Components Produced by Laser Powder Bed Fusion (L-PBF) Process. *Virtual Phys. Prototyp.* **2018**, *13*, 191–202. [CrossRef]
47. Berger, R. *Additive Manufacturing—A Game Changer for the Manufacturing Industry?* Roland Berger Strategy Consultants GmbH: Munich, Germany, 2013.